Quantum decoherence in high-order harmonic generation from solids

Gan Wang and Tao-Yuan Du*
School of Mathematics and Physics, China University of Geosciences, Wuhan 430074, China

(Received 5 November 2020; revised 11 May 2021; accepted 2 June 2021; published 14 June 2021)

For the high-order harmonic generation (HHG) from solids, the dephasing process induced by many-body interactions has been discussed extensively in the studies of using the semiconductor Bloch equations (SBEs). However, the role of dephasing in solid HHG is always ignored in the simulations of using a time-dependent Schrödinger equation under the independent electron approximation. To solve this problem, we introduce the imaginary potential to phenomenologically depict the dephasing process in the solid HHG. Compared with the results of experiment and SBEs, the validity of this approach has been verified by the laser intensity- and wavelength-dependent HHG spectra. Diffusion of the quantum wave packet controls the time-frequency characteristic in solid HHG. To obtain semiclassical trajectories whose predictions are consistent with the quantum simulations, we propose an open-trajectory model by relaxing the zero displacement condition in the tunneling and recollision steps. In addition, the quantum decoherence adjusts the chirp of the emission time profile via modulating the coherent overlap between recombined wave packets, which further paves a way to generate an attosecond pulse from solids and probe the dephasing time via the high-harmonic spectroscopy.

DOI: 10.1103/PhysRevA.103.063109

I. INTRODUCTION

High-order harmonic generation (HHG) is an extremely nonlinear optical process in which many photons of the driving laser field are up-converted to one higher-energy photon [1–6]. HHG in solids has attracted great attention since its experimental observation in 2011 [7–9]. The three main theoretical approaches to study solid-state HHG include (i) the time-dependent Schrödinger equation (TDSE), (ii) the time-dependent density functional theory (TDDFT), and (iii) the semiconductor Bloch equations (SBEs). The approaches such as TDSE and TDDFT ignore the effect of dephasing time [10–24]. Therefore, in the previous studies exploiting the first two approaches, the ultrafast dynamics of quantum wave packets exclude the phase-breaking processes induced by the many-body scattering effect in condensed matter.

Three- and four-step models have been proposed to understand the solid HHG process. The generalized three-step model can be summarized as the first ionization step, subsequent acceleration step of the ionized electron wave packet in an intense field, and recombination step of the electron wave packet with hole of any lattice sites [1–3]. However, before the first step of ionization, the electrons from the different initial states will be accelerated in the valence band and they can further efficiently tunnel to the conduction band. Thus, a new four-step model was established by including this pre-acceleration prior to tunnel ionization [25]. According to the introduced models, there are different trajectories that contribute to each individual harmonic order. The quantum interference effects between short and long trajectories have been reported experimentally in the HHG from the sapphire target [26]. In addition, the laser intensity- and wavelength-dependent HHG yield modulation, spectral splitting, and unexpected orientation of the polarization-resolved high-harmonic spectroscopy have been theoretically attributed to the quantum-trajectory interference [26–28]. And the rapid dephasing of the electron population plays a significant role in quantum-trajectory interference.

Dephasing time was introduced phenomenologically in the SBEs and led to the quantum decoherence of trajectories caused by the strong electron-particle scatterings [29]. Considering the deficiency of the single-active-electron (SAE) approximation adopted in the TDSE and TDDFT approaches and the difficulties associated with representing electronic and electron-phonon interactions in the SAE approximation, how to include the quantum decoherence in the time-dependent dynamics of the electron wave packet is intensively required. In addition, the partial conclusions in the studies of adopting the TDSE and TDDFT approaches are incomplete due to the lack of discussions of dephasing [18–24]. One should note that the dephasing controls the electron population distribution in the higher-lying energy bands of the excited band-gap materials. For instance, the step-by-step interband transitions and Bloch oscillations of the electron wave packet will be destroyed [11–13]. The reported phenomena, which lack discussions on dephasing, such as HHG yield enhancement (modulation) and energy band reconstruction shall be revisited with inclusion of the role of dephasing [15–19,22–24].

This paper is organized as follows. In Sec. II, we describe the method of introducing dephasing into the TDSE for the HHG process, by adding an imaginary potential to the Hamiltonian of the system, and present the numerical method in our simulations. In Sec. III, we demonstrate the validity of the method in the solid HHG and modify the closed-trajectory

*Corresponding author: duty@cug.edu.cn

model via relaxing two zero displacements in the tunneling and recollision steps, i.e., the so-called open-trajectory model. In addition, we discuss the role of dephasing on the dynamics of the quantum wave packet and the chirp of emission times. We summarize our work in Sec. IV. Atomic units are used throughout this work, unless specified otherwise.

II. THEORETICAL APPROACH

In the study of solid HHG, it is acceptable to simulate the semiconductors as an ensemble of noninteracting electrons characterized by a one-particle Hamiltonian $\hat{h}_0$. In our simulations, wave functions are expanded by Bloch states $|\phi_k^n\rangle$, which are the eigenstates of the field-free Hamiltonian $\hat{h}_0 = \frac{\hat{p}^2}{2} + V(x)$, described as

$$\hat{h}_0|\phi_k^n\rangle = E_n(k)|\phi_k^n\rangle. \tag{1}$$

We choose the one-dimensional periodic potential wells of the ZnO model along the specifically polarized direction, the form of which is $V(x) = -V_0[1 + \cos(\frac{2\pi}{a_0}x)]$, with $V_0 = 0.37$ a.u. and lattice constant $a_0 = 8$ a.u. [30].

The quantum decoherence induced by the disorder in real material [31,32], the propagation of a radiation field [33,34], and the electron-electron and electron-phonon scatterings [35,36] are totally neglected in the TDSE simulations of solid HHG. Decoherence can be referred to as a pure dephasing process and has been introduced phenomenologically in the SBE simulations via the term of the dephasing time [37]. To take account of this dephasing process in TDSE simulations of solid HHG, we introduce a non-Hermitian Hamiltonian including the one-particle Hamiltonian $\hat{h}_0$ and imaginary potential $-iU(x)$, which is written as

$$\hat{H}_0 = \frac{\hat{p}^2}{2} + V(x) - iU(x). \tag{2}$$

The eigenenergies of this non-Hermitian system become complex values $E_n(k) - i\Gamma_n(k)$, and $\Gamma_n(k)$ is called a dephasing rate for the band index n. The dephasing time is given as $T_2^n(k) = \frac{1}{2\Gamma_n(k)}$ [38]. The imaginary potential is physically related to the electron mean free path given by $T_2^n(k)v_n(k)$, where $v_n(k)$ is the group velocity of band index n. Note that the spatial range of $U(x)$ and value of U_0 determine the dephasing (or scattering) time T_2^n. As an example, with the choice of imaginary potential $U(x) = U_0[1 + \cos(\frac{2\pi}{10a_0}x)]$ and $U_0 = 0.0037$ a.u. [39], we display the real and imaginary energies of the non-Hermitian Hamiltonian and compare them with the energies of the Hermitian Hamiltonian in Fig. 1. One can observe that in Fig. 1(b), the dephasing rates $\Gamma_n(k)$ contributed by the imaginary potential for band index n are essentially k dependent, but almost constant here. In fact, when the imaginary potential we choose is constant, the dephasing time will also be constant. The effect of the k-dependent dephasing rate in solids, such as the trapezoidal envelope distribution in the Brillouin zone (BZ), has been discussed [40]. For simplicity, a constant imaginary potential will be used throughout this work and we subsequently drop the band index n and momentum k in the dephasing rate (time).

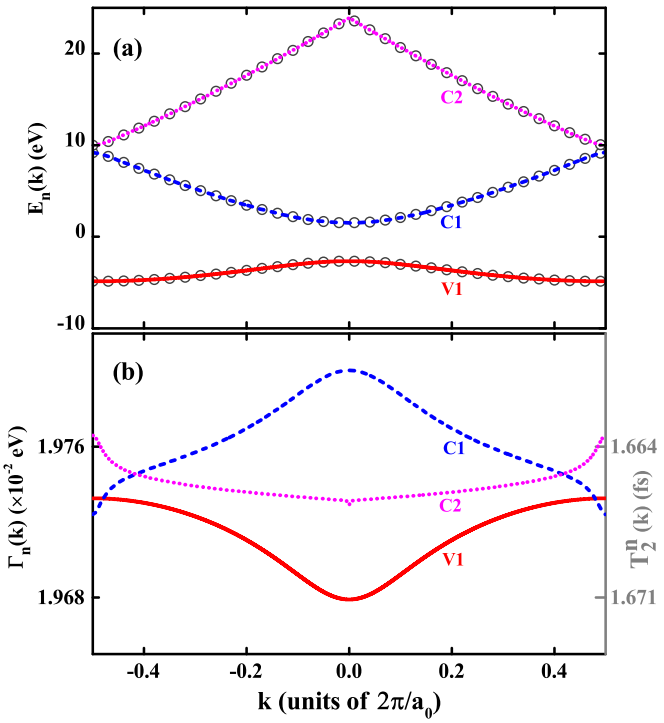

FIG. 1. (a) Real parts of the energy bands obtained by the diagonalizations of the non-Hermitian (dispersion curves) and Hermitian (gray dispersion circles) Hamiltonians. (b) Dephasing rates $\Gamma_n(k)$ introduced by the imaginary potential in Eq. (2).

Following the SAE approximation and velocity-gauge treatment, the TDSE can be written as

$$i\frac{\partial}{\partial t}|\Psi(t)\rangle = \left[\frac{[\hat{p} + A(t)]^2}{2} + V(x) - iU(x)\right]|\Psi(t)\rangle, \tag{3}$$

where the dipole approximation has been assumed. $A(t) = -\int_{-\infty}^{t} F(t')dt'$ is the vector potential with $\cos^2$ envelope. The wavelength and duration of the laser pulses are 2.0 μm and 16 optical cycles, respectively. To avoid the complicated electronic dynamics processes caused by the Bloch oscillation across the edge of the BZ, the laser intensity adopted in the following simulations is relatively moderate. Given the time-dependent Hamiltonian in Eq. (3), the evolution of the wave function can be written as

$$\begin{aligned}|\Psi_k(t_0 + \Delta t)\rangle &= e^{-i[\hat{H}_0 + A\hat{p} + A^2/2]\Delta t}|\Psi_k(t_0)\rangle \\ &= e^{-\Gamma\Delta t} \cdot e^{-i[\hat{h}_0 + A\hat{p} + A^2/2]\Delta t}|\Psi_k(t_0)\rangle.\end{aligned} \tag{4}$$

In Eq. (4), one will find that the wave function is attenuated by the imaginary potential at a rate of Γ, which takes account of many-body scatterings phenomenologically and is beyond the SAE approximation.

The time-dependent wave function in a basis of Bloch states is expressed as

$$|\Psi_k(t)\rangle = \sum_n C_k^n(t)|\phi_k^n\rangle. \tag{5}$$

Here, $k = k_0 - A$, reflecting that the vector potential in a given direction is the momentum that would be imparted to an electron starting from k_0. Electrons around the top of the valence

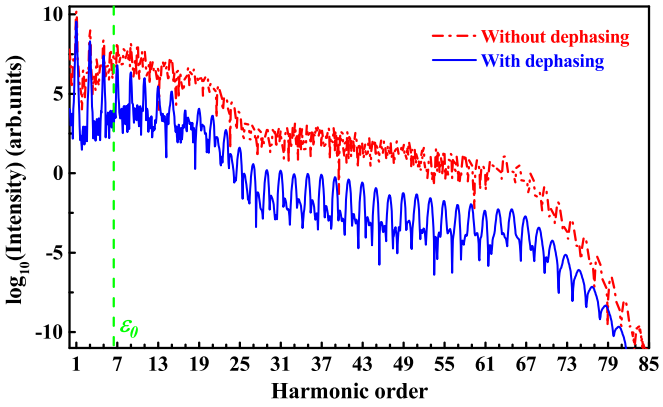

FIG. 2. High-order harmonic spectra with and without dephasing. The laser intensity, duration, and wavelength are 1.8 TW/cm^2, 16 optical cycles, and 2.0 μm, respectively. The laser optical cycle is $T_0 = 6.7$ fs. Dephasing times $T_2 = \infty$ (red dash-dotted line) and $T_0/4$ (blue solid line) are shown. The minimal gap (ε_0) is denoted by the green dashed vertical line.

band have maximal tunneling probability to be pumped into the conduction band, and the holes are left in the valence band. We choose the initial wave packet constructed by the Bloch states within the range of the $\pm 10\%$ BZ area near the $k_0 = 0$ point [41], and thus the initial wave packet holds a spatial localization to some extent. Making an insight into the time-dependent wave function of Eq. (5) in coordinate space, one can comprehend that the intra- and interband transitions in the HHG processes correspond to the motions of the Bloch wave packets moving at group and phase velocities, respectively [22]. Then we calculate the laser-induced current $J(t)$ as the coherent sum of the currents for the different initial states, which is written as

$$J(t) = -\int_{\mathrm{BZ}} [\langle \Psi_{\mathrm{k}}(t)|\hat{p}|\Psi_{\mathrm{k}}(t)\rangle] dk + A(t), \tag{6}$$

where the time-dependent wave functions $|\Psi_{\mathrm{k}}(t)\rangle$ are obtained by the Crank-Nicolson method [42]. The harmonic spectrum $I(\omega)$ could be obtained as the modulus square of the Fourier transform of the time-dependent current $J(t)$, which consists of the intra- and interband currents and had been clarified to be the dominated contribution from the interband current [11,14]. Before the Fourier transform, we multiply $J(t)$ by a Hanning window to increase the signal-to-noise ratio.

III. RESULTS AND DISCUSSIONS

First, to prove the reliability of treating quantum decoherence with an imaginary potential, we obtain the high-harmonic spectrum by solving the above-mentioned TDSE, which can include the phase-breaking process of the quantum wave-packet dynamics. As shown by the red dash-dotted curve in Fig. 2, the high-harmonic spectrum with the bad signal-to-noise ratio just displays the plateau structure in which the harmonic peaks are obscure. However, for the case of considering the dephasing introduced in Eq. (3), one can further observe that the high-harmonic spectrum shown by the blue solid curve presents a good signal-to-noise ratio and clear peak structure of the harmonics, which can also be acquired in SBE simulations with appropriate dephasing times [37].

To clarify the role of quantum decoherence in the HHG from solids driven by the intense laser pulses, we then make a classical-trajectory analysis on the HHG, shown in Fig. 2. According to the three-step model of the atomic system, an electron ionized at the certain moments t' usually can recombine and emit the same photon energy of the harmonic at several moments t. Excursion time, a characteristic parameter describing the trajectory of the electron-hole pair, is defined as $\tau = t - t'$. The trajectories of possessing an excursion time greater than one optical cycle are the so-called higher-order recollision trajectories. Thus the drifting electron wave packet with higher-order recollision trajectories experiences the longer excursion times τ, which leads to the fact that the contributions of high-order recollision trajectories in solid HHG are greatly suppressed at the decay rate $e^{-\tau/T_2}$. When the dephasing time T_2 is shorter than one-half of an optical cycle, the contributions from the multiple recollision trajectories will be negligible. Thus, only the first-recollision short and long trajectories whose excursion times are less than an optical cycle dominate the signals of HHG.

Considering the larger excursion time τ of the long trajectory resulting in the rapid decay rate term $e^{-\tau/T_2}$, the contribution from the long trajectory further becomes negligible. When the dephasing time is comparable with one-quarter of the optical cycle, only the short trajectory dominates the harmonic emissions in each half optical cycle, which results in the fact that the peaks of the odd harmonics get cleaner, as shown by the blue solid line in Fig. 2. Thus, the high-harmonic spectrum is elaborately dependent on the dephasing time.

In the present experimental setup, the role of quantum decoherence in solid HHG can be observed by the tunable parameters of laser pulses. Employing the methodology in which we have introduced quantum decoherence in the TDSE simulation, we show the high-order harmonic spectra as a function of the laser intensity and wavelength, as shown in Figs. 3(a) and 3(c), respectively. In Figs. 3(b) and 3(d), we obtain their corresponding yields by the integral in the first HHG plateau, as depicted by the blue solid curves. To compare with the case excluding decoherence, we further present their integral yields with the red dotted curves in Figs. 3(b) and 3(d). One can observe that the harmonic yields excluding decoherence are obviously modulated by laser intensity and wavelength, which has been attributed to the subcycle interference within an optical cycle and discussed in Ref. [27]. The blue solid curves in Figs. 3(b) and 3(d) uncover the role of decoherence on the suppression of subcycle interference, which reaches a good agreement with the experimental observations [7,43–45] and SBEs simulations [27]. Thus, the validity of our introducing a non-Hermitian Hamilton to include the wave-packet decoherence is demonstrated. In addition, for the blue solid line in Fig. 3(d), one can further observe that a slight yield oscillation within the wavelength range of 2.0–3.25 μm appears by comparing it within the wavelength range of 3.25–4.5 μm. The change of the harmonic yield modulation provides a way to retrieve the dephasing time of the Bloch electron wave packets in condensed matter [46].

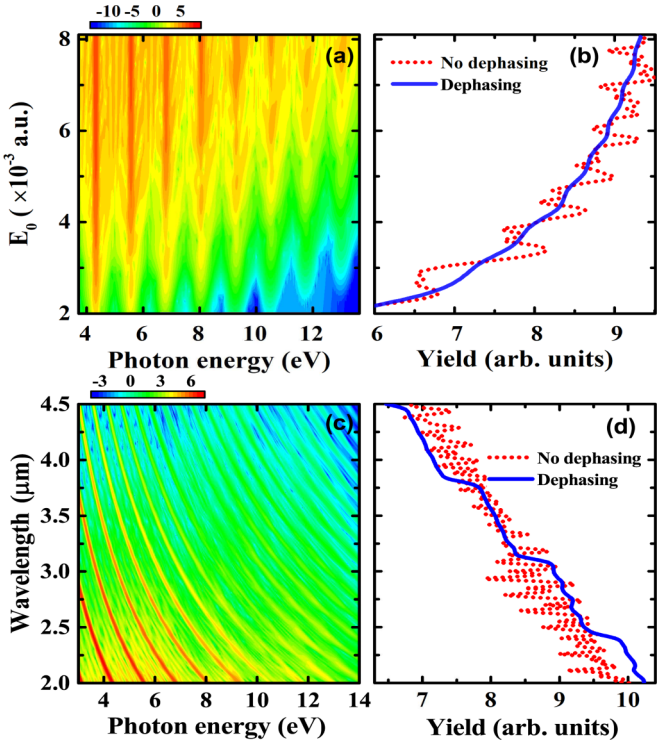

FIG. 3. Yield modulations varying with the electric field and wavelength of the laser pulses. The wavelength 2.0 μm and dephasing time $T_2 = 1.2$ fs are adopted in (a). For (c), the laser intensity and dephasing time are 1.8 TW cm^{-2} and $T_2 = 1.7$ fs, respectively. The corresponding yields via the integral within the range of the first plateau zone are shown in (b) and (d), in which the red dotted and the blue solid curves denote the results without and with dephasing, respectively.

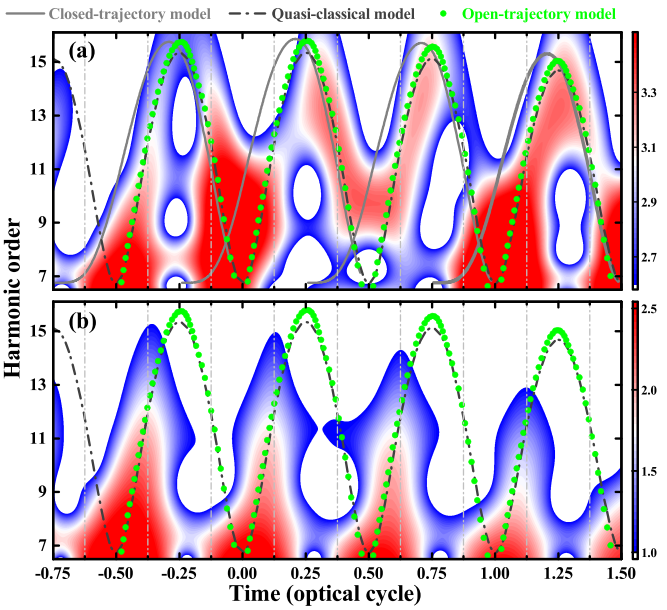

FIG. 4. Time-frequency analyses of the high-harmonic spectrum shown in Fig. 2 are presented by color scale in (a) and (b), respectively. The dephasing times T_2 adopted in (a) and (b) are ∞ and $T_0/4$ (1.7 fs), respectively. The gray solid curve and green solid circles denote the predicted emission times by the closed-trajectory and open-trajectory models, respectively. The dark-gray dash-dotted curve is the emission times given by the quasiclassical model in k space.

Next we set our sights on the comparisons between quantum simulations and semiclassical trajectory predictions. To intuitively understand the effect of dephasing time on the HHG process, we present the time-frequency analyses shown by the color diagrams of Figs. 4(a) and 4(b) [47]. One can find that the contribution of the long trajectory is extremely suppressed when the role of decoherence is included, as shown in Fig. 4(b) compared to Fig. 4(a). In view of this physical picture, the dephasing time can be understood as the time interval between each of the two scattering events. A shorter dephasing time will lead to the faster decay rate on the long trajectory and give rise to the survival of short trajectories, which guarantees the temporal coherence of emission events between each half optical cycle.

In the reciprocal space, the quasiclassical model describes the generation of high-order harmonics as follows [11–13]: (i) the electrons near $k_0 = 0$ with the minimal band gap are pumped from the top of the valence band into the conduction band and leave the holes in the valence band, (ii) the electrons and holes oscillate in their respective bands and follow their motion equation $k(t)$, (iii) electrons of the conduction bands recombine with the holes left in the valence band and emit high-order harmonics with band-gap energy $\varepsilon_g[k(t)]$. In Figs. 4(a) and 4(b), the quasiclassical prediction of HHG is presented by the dark-gray dash-dotted curve. One could observe that the results of the quasiclassical prediction reach a strong agreement with those of the quantum simulations.

In real space, to simplify the semiclassical trajectory analysis of solid HHG, the first-recollision trajectories, i.e., short and long trajectories, are taken into account. Under the picture of HHG in real space, the electron-hole pair generated at the moment t' possesses zero relative displacement. Then electron and hole wave packets propagate with their respective group velocities, $v_n = \nabla_k E_n[k(t)]$ $(n = c, v)$. Finally, the high harmonics with photon energy $\varepsilon_g[k(t)]$ are emitted when the excited electron and corresponding hole recombine with each other in real space. Here, the relative displacement between the electron and hole is denoted as

$$\Delta x_e - \Delta x_h = \int_{t'}^{t} v_g[k(t'')]dt'', \tag{7}$$

where Δx_e (Δx_h) represents the displacement of electrons (holes) from t' to t and $v_g = v_c - v_v$ is their velocity difference. Note that the emission of HHG in atomic and molecular systems must satisfy the condition of zero displacement in the tunneling and recombination steps, i.e., the so-called closed-trajectory model. The emission times predicted by the closed-trajectory model in Fig. 4(a) are obviously inconsistent with the results of the quantum simulation and quasiclassical prediction, as shown by the gray solid curve compared with the color diagram and dark-gray dash-dotted curve.

To understand the discrepancy between the closed-trajectory predictions and quantum simulations, we introduce an open-trajectory model by relaxing two conditions. As shown in Fig. 5, the open-trajectory model can be described as

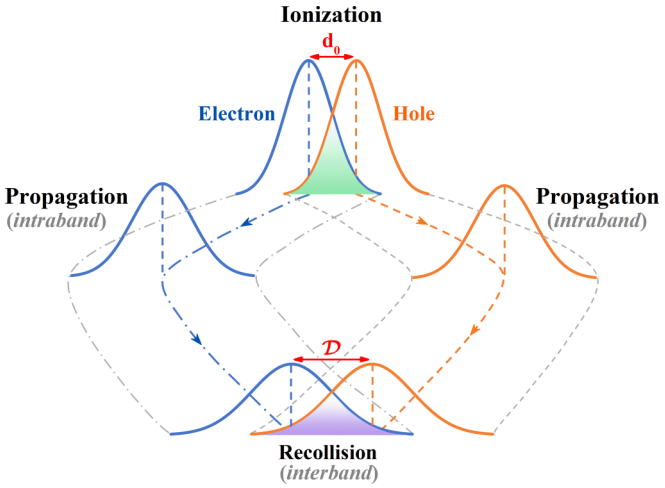

FIG. 5. Schematics of the open-trajectory model in the coordinate space. The corrections in which there are nonzero displacements in the tunneling and recombination steps and the wave-packet diffusion in the propagation process are considered here. d_0 and $\mathcal{D}$ denote the nonzero displacements in the tunneling and recombination steps, respectively. Change of the width of the electron and hole wave packets denotes the diffusion induced by propagation and many-body scatterings. Here the propagation and recollision can be understood as the intra- and interband transition dynamics in the reciprocal space, respectively.

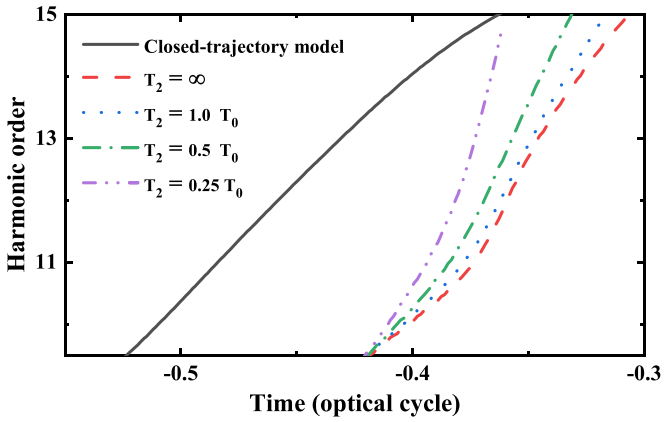

FIG. 6. The emission times of the short trajectory obtained from the quantum simulations vary with the dephasing times (T_2) of changing from ∞ to 0.25 T_0, where T_0 is the laser optical cycle. The laser parameters adopted here are the same as Fig. 2. The black solid line is the emission time predicted by the closed-trajectory model.

follows: (i) There is a spatial displacement between the electron and hole in the tunneling step [48], which is similar to the classical tunnel exit [49] for atomic and molecular systems. Thus one can relax the zero displacement in the generation step of the electron-hole pair. (ii) The electron and hole wave packets propagate and diffuse in real space. (iii) Considering the delocalization of wave packets and their quantum coherent overlap, one can further adjust the recollision condition with a nonzero displacement [46,50,51].

Under the conservation of energy, we can obtain a spatial displacement d_0 of the electrons by $d_0 = -\epsilon_g/F$ in the laser-assisted tunneling step [49]. Here the value of d_0 is adopted as $2a_0$, and the direction of d_0 is opposite to the polarized direction of the electric fields. Another parameter, a coherent-overlap length ($\mathcal{D}$) for the recollision step, is determined by the extent of the wave-packet diffusion, which is usually characterized by the dephasing time and driven laser pulse parameters and described as the relation $\mathcal{D} = \frac{4U_p}{A_0\Gamma} \propto F\lambda T_2$, which is substantiated in the Appendix. U_p, λ, and A_0 are the ponderomotive energy, driven-laser wavelength, and maximum momentum obtained from the driving field, respectively. Here the nonzero distances of recollision $\mathcal{D}$ are about $2a_0$. As a consequence, Eq. (7) can be rewritten as

$$\Delta x_e - \Delta x_h = \mathcal{D} - d_0. \tag{8}$$

Taking account of the polarization energies induced by the two nonzero displacements of the electron-hole pair at ionization and recollision steps, the photon energy Ω is modified as

$$\Omega = \varepsilon_g[k(t)] + F(t)\mathcal{D} - F(t')d_0. \tag{9}$$

One can find that the emission times (green solid circles) predicted by this open-trajectory model reach a strong agreement with the results of the time-frequency analyses and quasiclassical model, as shown in Figs. 4(a) and 4(b). The open-trajectory model provides an essential route to understand the quantum coherence between wave packets in solids driven by the laser pulses.

In addition to the above-mentioned spectroscopic characteristics of HHG, one can further delicately observe the change on the chirp of the short trajectory in Fig. 4(b) compared with Fig. 4(a). For the high harmonics contributed by the short trajectory, the difference of their emission times becomes smaller with the decrease of dephasing time. Here we provide a qualitative theoretical analysis to explain this phenomenon based on the perspective of quantum wave-packet propagation and diffusion. In the framework of wave-function representation, an excited wave packet will spontaneously spread during its propagation in periodic potentials. In this process, the quantum wave packets will undergo the transition from localization to the relatively spatial delocalization, as shown in Fig. 5. In the absence of dephasing, there is enough time for quantum wave packets to realize the spatial spread, which means that the coherent overlap (recombination) between the electron and hole wave packets is considerable, and then the open trajectories will appear. As a characteristic parameter controlling the coherent length between the electron and hole wave packets, the dephasing time determines the diffusion and survival of quantum trajectories. When a small dephasing time is employed, the quantum wave packet possesses a short coherent length in the recombination process of the electron-hole pairs. Thus the electron and hole will act as a "particle," and their paths of motion are closer to the results of the closed-trajectory model. As further demonstrated by Fig. 6, the emission times of the short trajectory are closer to the prediction of the closed-trajectory model when the dephasing time decreases. Based on the physical origin of dephasing, it is feasible to control the dephasing time via changing the degree of disorder, carrier concentration, thickness, and temperature in the solid materials. Optimization of

the dephasing time provides a route to control the emission times of HHG and further generates shorter attosecond pulses from solid HHG.

IV. CONCLUSION

In conclusion, we propose a methodology employing a non-Hermitian Hamiltonian to describe the dephasing process in high-harmonic generation from solids. The validity of this non-Hermitian Hamiltonian has been verified by the laser intensity- and wavelength-dependent HHG spectra via comparing it with the results of experiment and SBEs. To understand the discrepancy of emission times predicted by the closed-trajectory model and quantum simulation, we introduce an open-trajectory model and provide insight into the role of dephasing in the dynamics of quantum wave packets. Quantum decoherence controls the survival of quantum trajectories and modulates the diffusion of quantum wave packets in real space. In addition, the dephasing makes an impact on the coherent overlap between the electron and hole wave packets, which adjusts the chirp of the short trajectory, and paves a way to retrieve the coherent time in condensed matter and generate the isolated attosecond pulse.

ACKNOWLEDGMENTS

The authors thank C. Chen and J. A. Crosse very much for useful discussions. This work is supported by the National Natural Science Foundation of China (NSFC) (Grant No. 11904331).

APPENDIX: WAVE-PACKET DIFFUSION INDUCED BY DEPHASING

The electron-hole pair wave function can be denoted as

$$P(k,t) = -\int_0^\infty d\tau\, e^{iS(k,t,\tau)-i\omega t}\zeta, \tag{A1}$$

with the classical action given by

$$\begin{aligned} S(k,t,\tau) &= -\int_{t-\tau}^{t} dt'\, \Delta E(k,t') + i\Gamma\tau + \omega t \\ &= -\int_{t-\tau}^{t} dt'\, \{2U_p[\frac{k}{A_0} - \sin(\omega t')]^2\} + i\Gamma\tau + \omega t. \end{aligned} \tag{A2}$$

Here, ζ is the Rabi frequency of multiplying the electric field amplitude and transition dipole moment, $\Delta E = \frac{k^2}{2m_R}$ is the energy dispersion of the electron-hole pair under the excitation resonant and parabolic approximations, and m_R is the electron-hole reduced mass. $k(t) = k_0 - A_0\sin(\omega t)$ is the canonical momentum of the electron-hole pair, and $U_p = A_0^2/4m_R$ is the ponderomotive energy. We first expand Eq. (A2) and neglect the indirect driving term with the 2ω frequency component. Then we obtain the saddle-point equation by the first derivative of classical action S with respect to the recollision time t, which can be written as

$$\omega_s = 2U_p\{\sin[\omega(t-\tau)] - \sin(\omega t)\}^2. \tag{A3}$$

Finally, the highest energy can be obtained at the condition for $\omega t = 3\pi/2$ and $\omega\tau = \pi$. To obtain an estimate of the wave-function diffusion width, we expand the trigonometric functions to the first order in $t-\tau$, where only the points of highest-energy electron-hole pair trajectories in Eq. (A3) are included. Evaluating the excursion time τ integral in Eq. (A1) approximatively gives rise to the wave-function distribution in momentum space, which can be denoted as

$$P(k,t) \approx \frac{e^{iS(k,t)-i\omega t}\zeta}{2U_p(\frac{k^2}{A_0^2} + 2\frac{k}{A_0}) - i\Gamma}. \tag{A4}$$

Hence the half maximum of the wave function in the BZ appears at $k_{1/2} = -A_0(1 \pm \sqrt{1+\Gamma/2U_p})$ and then one achieves a full half maximum of $\Delta k_{\mathrm{FWHM}} = A_0\Gamma/2U_p$. The wave function width $\mathcal{D}$ can be given as $2/\Delta k_{\mathrm{FWHM}}$.

[1] P. B. Corkum, Phys. Rev. Lett. **71**, 1994 (1993).
[2] M. Lewenstein, P. Balcou, M. Y. Ivanov, A. L'Huillier, and P. B. Corkum, Phys. Rev. A **49**, 2117 (1994).
[3] B. Zaks, R. B. Liu, and M. S. Sherwin, Nature (London) **483**, 580 (2012).
[4] F. Krausz and M. Ivanov, Rev. Mod. Phys. **81**, 163 (2009).
[5] S. Y. Kruchinin, F. Krausz, and V. S. Yakovlev, Rev. Mod. Phys. **90**, 021002 (2018).
[6] K. A. Pronin and A. D. Bandrauk, Phys. Rev. Lett. **97**, 020602 (2006).
[7] S. Ghimire, A. D. DiChiara, E. Sistrunk, P. Agostini, L. F. DiMauro, and D. A. Reis, Nat. Phys. **7**, 138 (2011).
[8] G. Vampa, T. J. Hammond, N. Thiré, B. E. Schmidt, F. Légaré, C. R. McDonald, T. Brabec, and P. B. Corkum, Nature (London) **522**, 462 (2015).
[9] T. T. Luu, M. Garg, S. Yu. Kruchinin, A. Moulet, M. Th. Hassan, and E. Goulielmakis, Nature (London) **521**, 498 (2015).
[10] P. G. Hawkins, M. Y. Ivanov, and V. S. Yakovlev, Phys. Rev. A **91**, 013405 (2015).
[11] M. Wu, S. Ghimire, D. A. Reis, K. J. Schafer, and M. B. Gaarde, Phys. Rev. A **91**, 043839 (2015).
[12] M. Wu, D. A. Browne, K. J. Schafer, and M. B. Gaarde, Phys. Rev. A **94**, 063403 (2016).
[13] T.-Y. Du and X.-B. Bian, Opt. Express **25**, 151 (2017).
[14] T.-Y. Du, Z. Guan, X.-X. Zhou, and X.-B. Bian, Phys. Rev. A **94**, 023419 (2016).
[15] J.-B. Li, X. Zhang, S.-J. Yue, H.-M. Wu, B.-T. Hu, and H.-C. Du, Opt. Express **25**, 18603 (2017).
[16] X. Liu, X. Zhu, P. Lan, X. Zhang, D. Wang, Q. Zhang, and P. Lu, Phys. Rev. A **95**, 063419 (2017).
[17] J.-Z. Jin, X.-R. Xiao, H. Liang, M.-X. Wang, S.-G. Chen, Q. Gong, and L.-Y. Peng, Phys. Rev. A **97**, 043420 (2018).
[18] C. Yu, K. K. Hansen, and L. B. Madsen, Phys. Rev. A **99**, 063408 (2019).
[19] C. Yu, K. K. Hansen, and L. B. Madsen, Phys. Rev. A **99**, 013435 (2019).
[20] K. K. Hansen, T. Deffge, and D. Bauer, Phys. Rev. A **96**, 053418 (2017).

[21] K. K. Hansen, D. Bauer, and L. B. Madsen, Phys. Rev. A **97**, 043424 (2018).
[22] T.-Y. Du, X.-H. Huang, and X.-B. Bian, Phys. Rev. A **97**, 013403 (2018).
[23] J.-Z. Jin, H. Liang, X.-R. Xiao, M.-X. Wang, S.-G. Chen, X.-Y. Wu, Q. Gong, and L.-Y. Peng, J. Phys. B **51**, 16LT01 (2018).
[24] T.-Y. Du and S.-J. Ding, Phys. Rev. A **99**, 033406 (2019).
[25] L. Li, P. Lan, X. Zhu, T. Huang, Q. Zhang, M. Lein, and P. Lu, Phys. Rev. Lett. **122**, 193901 (2019).
[26] Y. W. Kim, T.-J. Shao, H. Kim, S. Han, S. Kim, M. Ciappina, X.-B. Bian, and S.-W. Kim, ACS Photon. **6**, 851 (2019).
[27] T.-Y. Du, D. Tang, and X.-B. Bian, Phys. Rev. A **98**, 063416 (2018).
[28] T.-Y. Du, Opt. Lett. **46**, 2007 (2021).
[29] G. Vampa, C. R. McDonald, G. Orlando, D. D. Klug, P. B. Corkum, and T. Brabec, Phys. Rev. Lett. **113**, 073901 (2014).
[30] J. C. Slater, Phys. Rev. **87**, 807 (1952).
[31] K. Chinzei and T. N. Ikeda, Phys. Rev. Research **2**, 013033 (2020).
[32] G. Orlando, T.-S. Ho, and S.-I. Chu, J. Opt. Soc. Am. B **37**, 1540 (2020).
[33] I. Kilen, M. Kolesik, J. Hader, J. V. Moloney, U. Huttner, M. K. Hagen, and S. W. Koch, Phys. Rev. Lett. **125**, 083901 (2020).
[34] L.-J. Lü and X.-B. Bian, Phys. Rev. A **102**, 033110 (2020).
[35] S. de Vega, J. D. Cox, F. Sols, and F. J. Garcia de Abajo, Phys. Rev. Research **2**, 013313 (2020).
[36] H. Nishidome, K. Nagai, K. Uchida, Y. Ichinose, Y. Yomogida, Y. Miyata, K. Tanaka, and K. Yanagi, Nano Lett. **20**, 6215 (2020).
[37] G. Vampa, C. R. McDonald, G. Orlando, P. B. Corkum, and T. Brabec, Phys. Rev. B **91**, 064302 (2015).
[38] J. P. Sun, G. I. Haddad, P. Mazumder, and J. N. Schulman, Proc. IEEE **86**, 641 (1998).
[39] L. Liu, J. Zhao, W. Dong, J. Liu, Y. Huang, and Z. X. Zhao, Phys. Rev. A **96**, 053403 (2017).
[40] F. Langer, M. Hohenleutner, C. Schmid *et al.*, Nature (London) **533**, 225 (2016).
[41] F. Navarrete, M. F. Ciappina, and U. Thumm, Phys. Rev. A **100**, 033405 (2019).
[42] X. B. Bian, Phys. Rev. A **90**, 033403 (2014).
[43] S. Ghimire, A. D. DiChiara, E. Sistrunk, U. B. Szafruga, P. Agostini, L. F. DiMauro, and D. A. Reis, Phys. Rev. Lett. **107**, 167407 (2011).
[44] Z. Wang, H. Park, Y. H. Lai *et al.*, Nat. Commun. **8**, 1686 (2017).
[45] G. Ndabashimiye, S. Ghimire, M. Wu *et al.*, Nature (London) **534**, 520 (2016).
[46] T.-Y. Du, Phys. Rev. A **100**, 053401 (2019).
[47] C. Chandre, S. Wiggins, and T. Uzer, Physica D (Amsterdam) **181**, 171 (2003).
[48] P. Jürgens, B. Liewehr, B. Kruse *et al.*, Nat. Phys. **16**, 1035 (2020).
[49] M. Geissler, G. Tempea, A. Scrinzi, M. Schnürer, F. Krausz, and T. Brabec, Phys. Rev. Lett. **83**, 2930 (1999).
[50] L. Yue and M. B. Gaarde, Phys. Rev. Lett. **124**, 153204 (2020).
[51] J. A. Crosse and R.-B. Liu, Phys. Rev. B **89**, 121202(R) (2014).